J|A|C|S ARTICLES

Published on Web 08/03/2010

Unique Electronic Structure Induced High Photoreactivity of Sulfur-Doped Graphitic C_3N_4

Gang Liu,[†] Ping Niu,[†] Chenghua Sun,[‡,§] Sean C. Smith,[§] Zhigang Chen,[‡] Gao Qing (Max) Lu,[‡] and Hui-Ming Cheng*[,†]

Shenyang National Laboratory for Materials Science, Institute of Metal Research, Chinese Academy of Sciences, 72 Wenhua Road, Shenyang 110016, China, ARC Centre of Excellence for Functional Nanomaterials, The University of Queensland, QLD 4072, Australia, and Centre for Computational Molecular Science, Australia Institute for Bioengineering and Nanotechnology, The University of Queensland, QLD 4072, Australia

Received May 4, 2010; E-mail: cheng@imr.ac.cn

Abstract: Electronic structure intrinsically controls the light absorbance, redox potential, charge-carrier mobility, and consequently, photoreactivity of semiconductor photocatalysts. The conventional approach of modifying the electronic structure of a semiconductor photocatalyst for a wider absorption range by anion doping operates at the cost of reduced redox potentials and/or charge-carrier mobility, so that its photoreactivity is usually limited and some important reactions may not occur at all. Here, we report sulfur-doped graphitic C_3N_4 ($C_3N_{4-x}S_x$) with a unique electronic structure that displays an increased valence bandwidth in combination with an elevated conduction band minimum and a slightly reduced absorbance. The $C_3N_{4-x}S_x$ shows a photoreactivity of H_2 evolution 7.2 and 8.0 times higher than C_3N_4 under $\lambda > 300$ and 420 nm, respectively. More strikingly, the complete oxidation process of phenol under $\lambda > 400$ nm can occur for sulfur-doped C_3N_4, which is impossible for C_3N_4 even under $\lambda > 300$ nm. The homogeneous substitution of sulfur for lattice nitrogen and a concomitant quantum confinement effect are identified as the cause of this unique electronic structure and, consequently, the excellent photoreactivity of $C_3N_{4-x}S_x$. The results acquired may shed light on general doping strategies for designing potentially efficient photocatalysts.

1. Introduction

Seeking highly active photocatalysts has been an intensifying endeavor worldwide, mainly due to their promising applications for renewable energy and clean environment.[1,2] So far, many impressive photocatalytic materials have been explored and have shown exciting photoreactivity.[3−6] Besides the demand for exploring new materials, the development of innovative strategies to enhance the reactivity of known potential photocatalysts is also playing an indispensible role in developing technologies. Among various strategies,[7] there is little doubt that doping, especially anion doping pioneered by Asahi et al.,[8a] is most widely investigated because of its effectiveness in broadening the light responsive range of wide-bandgap semiconductors.[9−11] For anion doping, two main hypotheses have been put forward at electronic structure level for the induced functionality (i.e., extended absorption range), namely, (i) formation of localized states from dopants in the bandgap and (ii) elevation of the valence band (VB) maximum through mixing of dopant states with the upper VB states of the bulk material. Which of the two mechanisms predominates depends on whether surface

[†] Institute of Metal Research, Chinese Academy of Sciences.
[‡] ARC Centre of Excellence for Functional Nanomaterials, The University of Queensland.
[§] Australia Institute for Bioengineering and Nanotechnology, The University of Queensland.

(1) Fujishima, A.; Honda, K. *Nature* **1972**, *238*, 37.
(2) Hoffmann, M. R.; Martin, S. T.; Choi, W.; Bahnemann, D. W. *Chem. Rev.* **1995**, *95*, 69.
(3) (a) Zou, Z. G.; Ye, J. H.; Sayama, K.; Arakawa, H. *Nature* **2001**, *414*, 625. (b) Yi, Z. G.; Ye, J. H.; Kikugawa, N.; Kako, T.; Ouyang, S.; Stuart-Williams, H.; Yang, H.; Cao, J. Y.; Luo, W. J.; Li, Z. S.; Liu, Y.; Withers, R. L. *Nat. Mater.* **2010**, *9*, 559.
(4) Kato, H.; Asakura, K.; Kudo, A. *J. Am. Chem. Soc.* **2003**, *125*, 3082.
(5) (a) Maeda, K.; Teramura, K.; Lu, D. L.; Takata, T.; Saito, N.; Inoue, Y.; Domen, K. *Nature* **2006**, *440*, 295. (b) Maeda, K.; Higashi, M.; Lu, D. L.; Abe, R.; Domen, K. *J. Am. Chem. Soc.* **2010**, *132*, 5858.
(6) (a) Tada, H.; Mitsui, T.; Kiyonaga, T.; Akita, T.; Tanaka, K. *Nat. Mater.* **2006**, *5*, 782. (b) Tada, H.; Kiyonaga, T.; Naya, S. *Chem. Soc. Rev.* **2009**, *38*, 1849. (c) Abe, R.; Takami, H.; Murakami, N.; Ohtani, B. *J. Am. Chem. Soc.* **2008**, *130*, 7780. (d) Yan, H. J.; Yang, J. H.; Ma, G. J.; Wu, G. P.; Zong, X.; Lei, Z. B.; Shi, J. Y.; Li, C. *J. Catal.* **2009**, *266*, 165. (e) Zong, X.; Yan, H. J.; Wu, G. P.; Ma, G. J.; Wen, F. Y.; Wang, L.; Li, C. *J. Am. Chem. Soc.* **2008**, *130*, 7176.
(7) Liu, G.; Wang, L. Z.; Yang, H. G.; Cheng, H. M.; Lu, G. Q. *J. Mater. Chem.* **2010**, *20*, 831.
(8) (a) Asahi, R.; Morikawa, T.; Ohwaki, T.; Aoki, K.; Taga, Y *Science* **2001**, *293*, 269. (b) Livraghi, S.; Paganini, M. C.; Giamello, E.; Selloni, A.; Di Valentin, C.; Pacchioni, G. *J. Am. Chem. Soc.* **2006**, *128*, 15666. (c) Martinez-Ferrero, E.; Sakatani, Y.; Boissiere, C.; Grosso, D.; Fuertes, A.; Fraxedas, J.; Sanchez, C. *Adv. Funct. Mater.* **2007**, *17*, 3348. (d) Chen, X. B.; Burd, C. *J. Am. Chem. Soc.* **2008**, *130*, 5018. (e) Wang, J; Tafen, D. N.; Lewis, J. P.; Hong, Z. L.; Manivannan, A; Zhi, M. J.; Li, M; Wu, N. Q. *J. Am. Chem. Soc.* **2009**, *131*, 12290. (f) Li, X. K.; Kikugawa, N.; Ye, J. H. *Adv. Mater.* **2008**, *20*, 3816.
(9) (a) Khan, S. U. M.; Al-Shahry, M.; Ingler, W. B. *Science* **2002**, *297*, 2243. (b) Sakthivel, S.; Kisch, H. *Angew. Chem., Int. Ed.* **2003**, *42*, 4908.
(10) Umebayashi, T.; Yamaki, T.; Itoh, H.; Asai, K. *Appl. Phys. Lett.* **2002**, *81*, 454.
(11) Zhao, W.; Ma, W. H.; Chen, C. C.; Zhao, J. C.; Shuai, Z. G. *J. Am. Chem. Soc.* **2004**, *126*, 4782.

 10.1021/ja103798k

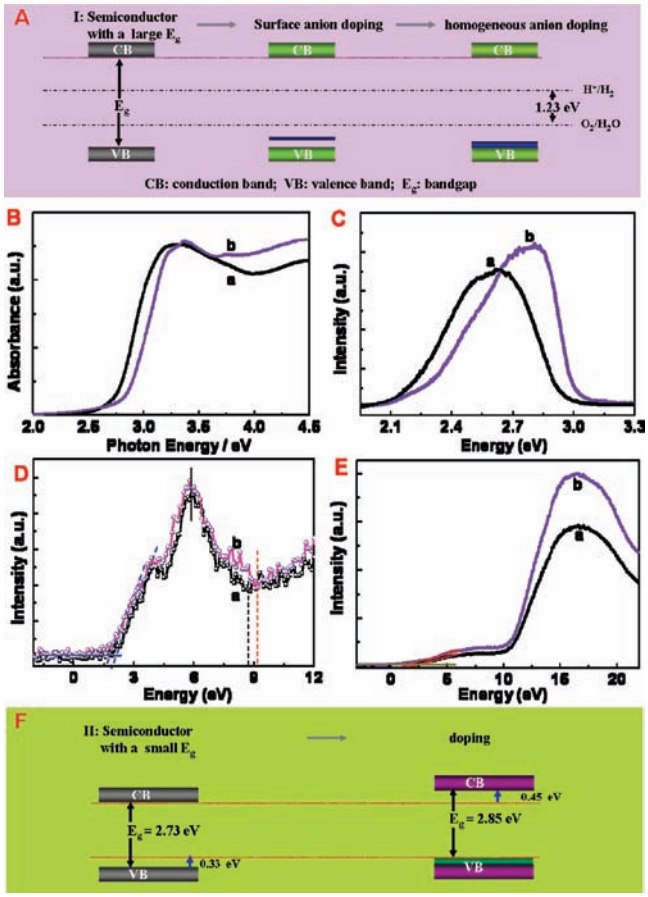

Figure 1. (A) Schematic of the modified band structures of semiconductor by surface and homogeneous anion doping; (B) UV−visible absorption spectra of C_3N_4 (a) and $C_3N_{4-x}S_x$ (b); (C) fluorescence emission spectra of C_3N_4 (a) and $C_3N_{4-x}S_x$ (b); (D) total densities of states of XPS valence band spectra of C_3N_4 (a) and $C_3N_{4-x}S_x$ (b); (E) ultraviolet photoelectron spectra of C_3N_4 (a) and $C_3N_{4-x}S_x$ (b); (F) schematic of the electronic structure of $C_3N_{4-x}S_x$ compared to that of C_3N_4.

doping or homogeneous doping is implemented at the atomic level,[7] as shown in Figure 1A.

An optimal semiconductor photocatalyst arises from a balance of several crucial parameters: absorbance, redox potentials, and mobility of photoinduced charge carriers. Although both mechanisms described in Figure 1A can effectively extend absorption range, some intrinsic drawbacks remain, including reduced mobility of electron holes in the localized states as well as lowered oxidative potential of electron holes, both of which are key factors that limit reactivity.[8a,12]

From the viewpoint of kinetic and thermodynamic requirements for photocatalytic reactions, two features are worthy of noting: the valence bandwidth and the conduction band minimum energy. The VB width intrinsically controls the mobility of holes: the wider the VB, the higher the mobility of holes generated, and thus, the better the photo-oxidation efficacy of holes. To increase the VB width by anion doping requires both a homogeneous distribution of the dopant throughout the bulk and that the dopant atom has a lower electronegativity than the substituted atom, for example, the homogeneous substitutional N for O in titanates.[7] However, the realization of homogeneous doping can be inherently restricted due to the limited thermodynamic solubility of substitutional dopants. Elevation of the conduction band (CB) minimum can also be crucial, not only in providing more reductive photoexcited electrons, but also inhibiting electron−hole recombination due to the rapid transfer of photoexcited electrons to reactants. The quantum confinement effect (QCE) in semiconductors is well-known for increasing the intrinsic bandgap by oppositely shifting valence and conduction band edges.[13] Although the QCE is not uncommon in some systems for modulating optical and catalytic properties,[13,14] its power is rarely exerted for most photocatalysts, in particular for doped photocatalysts, largely due to the difficulty of generating the very small critical particle size.[15]

The integration of these two favorable characteristics in a photocatalyst is rarely realized and is expected to be very powerful in achieving high overall reactivity. To achieve such a unique electronic structure, we have explored the utilization of layered C_3N_4 with a graphitic structure, which is recently recognized as a very promising metal-free photocatalyst.[16] Our strategy is based on the following rationales: (i) the layered structure with interlayer galleries should facilitate *homogeneous* doping of heteroatoms throughout the particles, thereby enabling the merging and coupling of the highest occupied dopant states into the upper edge of the VB and extending its width; (ii) particle size can be effectively tailored by decreasing both stacking number and sheet size; (iii) the relatively small bandgap (ca. 2.7 eV) of the undoped graphitic C_3N_4 can tolerate a modest increase of the bandgap by upshifting the CB minimum without affecting visible light response too much.

In this work, to demonstrate the above considerations, sulfur, which has a smaller electronegativity than nitrogen (2.58 vs 3.04),[7] was chosen as dopant into C_3N_4. The desirable electronic structural properties of the sulfur-doped C_3N_4 were evidenced by various spectroscopy characterizations. The remarkable electronic structure exhibits potency in achieving both high photoreduction and photo-oxidation reactivity. The origin of the unique electronic structure and, consequently, the excellent photoreactivity of the sulfur-doped C_3N_4 are explored both experimentally and theoretically, shedding light on general doping strategies for designing potentially efficient photocatalysts.

2. Experimental Section and Computational Details

2.1. Sample Preparation Procedure. Graphitic carbon nitride C_3N_4 was synthesized according to a reported procedure.[17] In detail, 6 g of dicyandiamide (Aldrich, 99%) was heated at 550 °C in air for 4 h with a ramping rate of 2.3 °C/min. The resultant yellow solid was milled into powder for the subsequent sulfur doping. To prepare sulfur-doped C_3N_4 ($C_3N_{4-x}S_x$), a certain amount of C_3N_4

(12) Linsebigler, A. L.; Lu, G. Q.; Yates, J. T, Jr. *Chem. Rev.* **1995**, *95*, 735.
(13) Alivisatos, A. P. *Science* **1996**, *271*, 933.
(14) Valden, M.; Lai, X.; Goodman, D. W. *Science* **1998**, *281*, 1647.
(15) Satoh, N.; Nakashima, T.; Kamikura, K.; Yamamoto, K. *Nat. Nanotechnol.* **2008**, *3*, 106.
(16) (a) Wang, X. C.; Maeda, K.; Thomas, A.; Takanabe, K.; Xin, G.; Carlsson, J. M.; Domen, K.; Antonietti, M. *Nat. Mater.* **2009**, *8*, 76. (b) Wang, X. C.; Chen, X. F.; Thomas, A.; Fu, X. Z.; Antonietti, M. *Adv. Mater.* **2009**, *21*, 1609. (c) Wang, X. C.; Maeda, K.; Chen, X. F.; Takanabe, K.; Domen, K.; Hou, Y. D.; Fu, X. Z.; Antonietti, M. *J. Am. Chem. Soc.* **2009**, *131*, 1680. (d) Zhang, J. S.; Chen, X. F.; Takanabe, K.; Maeda, K.; Domen, K.; Epping, J. D.; Fu, X. Z.; Antonietti, M.; Wang, X. C. *Angew. Chem., Int. Ed.* **2010**, *49*, 441. (e) Zhang, Y. J.; Thomas, A.; Antonietti, M. *J. Am. Chem. Soc.* **2009**, *131*, 50. (f) Wang, Y.; Zhang, J. S.; Wang, X. C.; Antonietti, M.; Li, H. R. *Angew. Chem., Int. Ed.* **2010**, *49*, 3356. (g) Zhang, Y. J.; Mori, T.; Ye, J. H.; Antonietti, M. *J. Am. Chem. Soc.* **2010**, *132*, 6294.
(17) Goettmann, F.; Fischer, A.; Antonietti, M.; Thomas, A. *Angew. Chem., Int. Ed.* **2006**, *45*, 4467.

powder was treated at 450 °C in gaseous H_2S atmosphere (purity 99.99%) with a flow rate of 12 mL/min for 1 h.

2.2. Characterization. X-ray diffraction (XRD) patterns of the samples were recorded on a Rigaku diffractometer using Cu irradiation. Their morphology was determined by transmission electron microscopy (TEM) performed on Tecnai F30. The Brunauer−Emmett−Teller (BET) surface area was determined by nitrogen adsorption−desorption isotherm measurements at 77 K (ASAP 2010). The optical absorbance spectra of the samples were recorded in a UV−visible spectrophotometer (JACSCO-550). Fluorescence emission spectrum was recorded at room temperature excited by incident light of 325 nm with a fluorescence spectrophotometer (Hitachi, F-4500). Chemical compositions and valence band spectra of C_3N_4 were analyzed using X-ray photoelectron spectroscopy (Thermo Escalab 250, a monochromatic Al K_α X-ray source). All binding energies were referenced to the C 1s peak (284.6 eV) arising from adventitious carbon. Ultraviolet photoelectron spectroscopy was used with the He II (40.8 eV) as energy source. The sulfur K-edge X-ray absorption near-edge structure (XANES) measurement of the sample was performed at the beamline 4B7A of Beijing Synchrotron Radiation Facility (BSRF). Sulfur K-edge spectrum was obtained on a double-crystal monochromator (DCM) and was recorded in X-ray fluorescence yield (XFY) mode.

2.3. Photoreactivity Measurements. Water splitting reactions were carried out in a top-irradiation vessel connected to a glass closed gas circulation system. A total of 100 mg of the photocatalyst powder was dispersed in 300 mL of aqueous solution containing 10% triethanolamine scavenger in volume. The decomposition of 6 wt % Pt cocatalyst was conducted by directly dissolving H_2PtCl_6 into the above 300 mL reaction solution.[16] The reaction temperature was maintained below 9 °C. The amount of H_2 evolved was determined using a gas chromatography (Agilent Technologies: 6890N). The detailed schematic of water splitting measurement equipment can be found in Wang et al.[18]

Photodegradation reactions of phenol were conducted by adding 100 mg of photocatalyst into 100 mL of 30 mg L^{-1} phenol solution. Before exposure to light irradiation, the suspension was stirred in dark for 30 min. Then, 5 mL of the solution was taken out every 30 min under $\lambda > 300$ nm or 2 h under $\lambda > 400$ nm, and centrifuged for UV−visible absorption spectrum measurements. During the photoreactions, no oxygen was bubbled into suspension. The concentration of phenol was determined by monitoring the change of optical density at 270 nm.

·OH radical reactions were performed as follows. Five milligrams of photocatalyst was suspended in 80 mL aqueous solution containing 0.01 M NaOH and 3 mM terephthalic acid. Before exposure to light irradiation, the suspension was stirred in dark for 30 min. Then, 5 mL of the solution was taken out every 5 min under $\lambda > 300$ nm or 10 min under $\lambda > 400$ nm, and centrifuged for fluorescence spectrum measurements. During the photoreactions, no oxygen was bubbled into the suspension. A fluorescence spectrophotometer (Hitachi, F-4500) was used to measure the fluorescence signal of the 2-hydroxy terephthalic acid generated. The excitation light employed in recording fluorescence spectra was 320 nm.

The light source was a 300 W Xe lamp (Beijing Trusttech Co. Ltd., PLS-SXE-300UV), whose emission spectrum is given in Figure S1. The wavelength of incident light in the photocatalytic reactions was satisfied by employing 400 nm, 420 nm long-pass glass filters and corresponding monochromatic glass filters.

2.4. Computational Parameters. Spin-polarized density functional theory (DFT) calculations were carried out using the DMol3 code.[19,20] The generalized gradient approximation (GGA) with the functional of Perdew−Burke−Ernzerhof functional (PBE)[21] was utilized for all geometric optimization and single-point energy calculations. Effective core potentials with double-numeric quality basis were employed for the description of core electrons. During our calculations, the convergence criteria for structure optimization were set to (1) energy tolerance of 1.0×10^{-6} Ha per atom, (2) maximum force tolerance of 1.0×10^{-4} Ha/Å, and (3) maximum displacement tolerance of 1.0×10^{-3} Å. The parameters for self-consistent field iterations for optimization (***energy calculations***) were set as: (1) energy tolerance of 5.0×10^{-6} Ha (***1.0 × 10⁻⁶ Ha***) and (2) Monkhorst-Pack **k**-point sampling: $5 \times 5 \times 3$. Larger sets of k points were tested, making sure that there is no significant change in the calculated energies when a larger number of k points were used.

3. Results and Discussion

3.1. Electronic Structure. UV−visible absorption spectra in Figure 1B indicate that the intrinsic absorption edge of C_3N_4 shows a blue-shift upon sulfur doping. The almost exactly parallel characteristics of the absorption edge of resultant $C_3N_{4-x}S_x$ to that of C_3N_4 strongly suggests the nature of band-to-band excitation in $C_3N_{4-x}S_x$. The bandgaps of C_3N_4 and $C_3N_{4-x}S_x$ determined are 2.73 and 2.85 eV. The evidenced shift of intrinsic fluorescence emission peak from 2.63 to 2.77 eV by sulfur doping (see Figure 1C) doubly confirms the enlarged bandgap of $C_3N_{4-x}S_x$.

To determine the effect of sulfur doping on relative positions of CB and VB edges and VB width of C_3N_4, the total densities of states of VBs (Figure 1D) were measured. In contrast to C_3N_4, the doped $C_3N_{4-x}S_x$ demonstrates a VB maximum up-shifted from 2.12 to 1.79 eV as well as the VB itself being widened. Intriguingly, the upward shift of the VB maximum by 0.33 eV is *not* accompanied by a decreased bandgap; rather, the bandgap is increased by 0.12 eV. The trend of VB maximum upshift is also evidenced in the recorded ultraviolet photoelectron spectra (UPS) of C_3N_4 and $C_3N_{4-x}S_x$ (See Figure 1E), though the observed shift from 2.16 eV to 1.72 by 0.44 eV is larger than 0.33 eV. This suggests that the doping has indeed induced a simultaneous upward shift of the CB minimum by 0.45 eV (the XPS VB spectra were employed to determine the band edges) as illustrated schematically in Figure 1F. Clearly, a unique electronic structure featuring an elevated CB minimum as well as a widened VB has been established in $C_3N_{4-x}S_x$.

3.2. Photoreduction and Photooxidaion Activity. The manipulation of electronic structure demonstrated above has important consequences for the photocatalytic activity of the $C_3N_{4-x}S_x$. Under $\lambda > 300$ nm (see Figure 2A), stable hydrogen evolution by $C_3N_{4-x}S_x$ was observed from photoreductive water splitting at a rate 7.2 times higher than that observed from the undoped C_3N_4. More importantly, stable hydrogen evolution from $C_3N_{4-x}S_x$ under $\lambda > 420$ nm (see Figure 2A) was observed to be 8.0 times faster than that from C_3N_4, despite the fact that the absorption range of $C_3N_{4-x}S_x$ is slightly decreased by 0.12 eV in comparison with C_3N_4 (Figure 1B). The excellent stability of hydrogen evolution with no N_2 release during irradiation can be attributed to the strong binding of N in the covalent carbon nitride,[16a] which can also be supported by the unchanged chemical states of these carbon based photocatalysts (see Figure S2). The wavelength dependence of hydrogen evolution from $C_3N_{4-x}S_x$ shown in Figure 2B is consistent with its optical absorption spectrum, with the maximum active wavelength for

(18) Wang, X. W.; Liu, G.; Chen, Z. G.; Li, F.; Lu, G. Q.; Cheng, H. M. *Chem. Commun.* **2009**, 3452.
(19) Delley, B. *J. Chem. Phys.* **1990**, *92*, 508.
(20) Delley, B. *J. Chem. Phys.* **2000**, *113*, 7756.
(21) Perdew, J. P.; Burke, K.; Ernzerhof, M. *Phys. Rev. B.* **1996**, *77*, 3865.

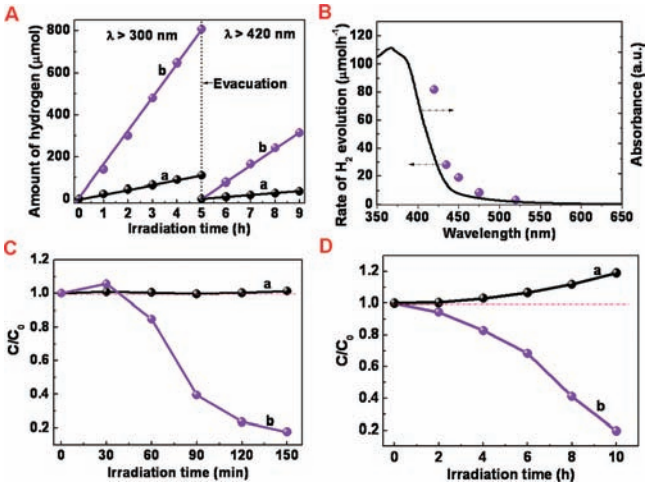

Figure 2. (A) A typical time course of hydrogen evolution from water containing 10 vol% triethanolamine scavenger by Pt-deposited C_3N_4 (a) and $C_3N_{4-x}S_x$ (b) under $\lambda > 300$ and 420 nm, respectively; (B) dependence of hydrogen evolution on wavelength by $C_3N_{4-x}S_x$. For comparison, UV−visible absorption spectrum of $C_3N_{4-x}S_x$ is also given. (C and D) Activity comparison of photo-oxidation process of phenol by C_3N_4 (a) and $C_3N_{4-x}S_x$ (b) under $\lambda > 300$ and 400 nm, respectively.

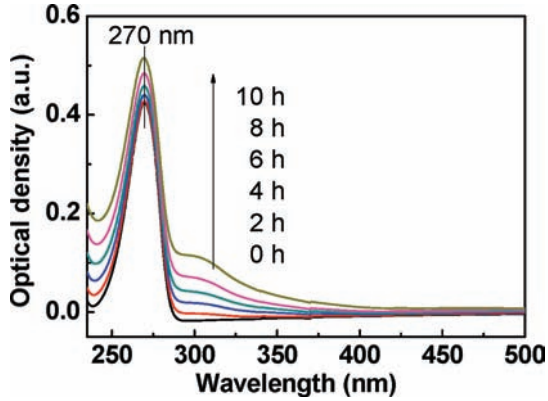

Figure 3. The photodegradation process of phenol in water with C_3N_4 under $\lambda > 400$ nm for 10 h.

hydrogen evolution in good agreement with the absorption edge of $C_3N_{4-x}S_x$.

In addition to the superior photoreduction capacity displayed by the $C_3N_{4-x}S_x$ as demonstrated above, a striking change in photo-oxidation capacity, associated with the generated electron holes, was also observed, by comparing the photodegradation behaviors of phenol with C_3N_4 and $C_3N_{4-x}S_x$. Under $\lambda > 300$ nm, phenol can be almost completely decomposed by $C_3N_{4-x}S_x$ within 150 min while no decomposition occurs at all with C_3N_4 (Figure 2C). Even under $\lambda > 400$ nm, more than 80% phenol molecules can be removed with $C_3N_{4-x}S_x$ within 10 h (Figure 2D). With C_3N_4, in contrast, an apparent concentration increase appears with prolonged irradiation. A similar concentration increase in the photodegradation of phenol was also reported in TiO_2 based photocatalysts.[22] Such an increase is attributed to the formation of certain intermediate species during the reaction, which gives a higher absorption at 270 nm for concentration measurements (see Figure 3). Actually, this intermediate species was also formed with the $C_3N_{4-x}S_x$ catalyst

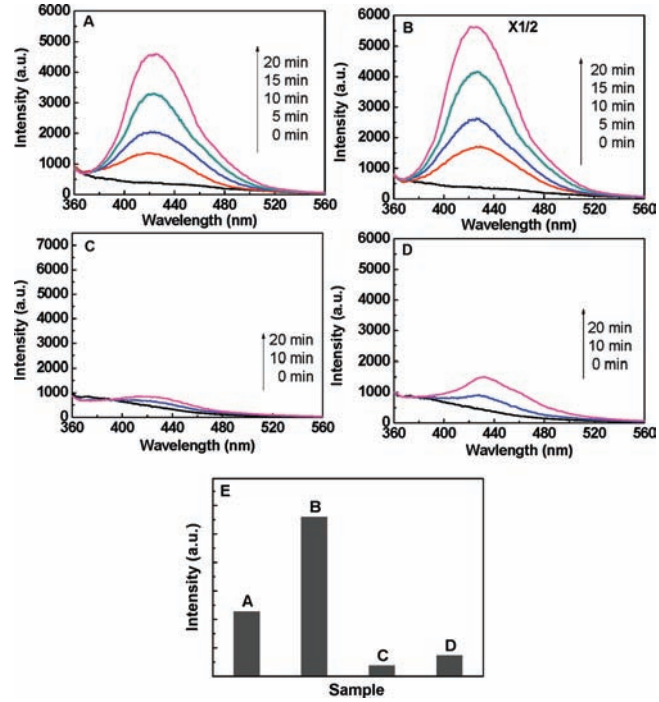

Figure 4. Fluorescence spectra of 2-hydroxy terephthalic acid (TAOH) solution generated by (A) C_3N_4 and (B) $C_3N_{4-x}S_x$ under $\lambda > 300$ nm; (C) C_3N_4 and (D) $C_3N_{4-x}S_x$ under $\lambda > 400$ nm in 3 mM terephthalic acid for 20 min. (E) Comparison of the amount of final TAOH generated for 20 min from A to D.

by showing an increased concentration at 30 min in Figure 2C-b. Therefore, the photodegradation of phenol proceeds with the formation and subsequent decomposition of intermediate species, which is in accordance with the reported multistep mechanisms of phenol photodegradation.[23] Our results suggest that both $C_3N_{4-x}S_x$ and C_3N_4 can cause the formation of intermediate species; however, the subsequent decomposition can occur very effectively with $C_3N_{4-x}S_x$ even under low energy irradiation ($\lambda > 400$ nm) but fail with C_3N_4 even under high energy irradiation ($\lambda > 300$ nm).

It is well-established that the photo-oxidation reactions of organic molecules can directly utilize the generated VB holes or the main generated active species, ·OH radicals, from the reaction of holes with surface adsorbed water or hydroxyl groups.[12] To qualitatively distinguish the involvement of holes and/or ·OH radicals in the oxidation of phenol, the capability of generating ·OH radicals of $C_3N_{4-x}S_x$ and C_3N_4 was compared by detecting the amount of 2-hydroxy terephthalic acid from the reaction of ·OH radicals with terephthalic acid.[24] $C_3N_{4-x}S_x$ shows only two times higher efficiency than C_3N_4 under either $\lambda > 300$ nm or $\lambda > 400$ nm (see Figure 4). This result indicates that the excellent capability of $C_3N_{4-x}S_x$ in decomposing phenol is mainly caused by the direct involvement of holes. Otherwise, a certain portion of phenol must have been decomposed by C_3N_4.

Generally, a larger surface area of photocatalysts can be favorable for photocatalytic reaction by providing more possible reaction sites.[25] The possible contribution of increased surface

(22) Wang, W. D.; Serp, P.; Kalck, P.; Luís Faria, J. *Appl. Catal., B* **2005**, *56*, 305.
(23) Sobczyński, A.; Duczmal, Ł.; Zmudziński, W. *J. Mol. Catal., A* **2004**, *213*, 225.
(24) Hirakawa, T.; Nosaka, Y. *Langmuir* **2002**, *18*, 3247.
(25) (a) Martinez-Ferrero, E.; Sakatani, Y.; Boissiere, C.; Grosso, D.; Fuertes, A.; Fraxedas, J.; Sanchez, C. *Adv. Funct. Mater.* **2007**, *17*, 3348. (b) Liu, G.; Sun, C. H.; Yang, H. G.; Smith, S. C.; Wang, L. Z.; Lu, G. Q.; Cheng, H. M. *Chem. Commun.* **2010**, *46*, 755.

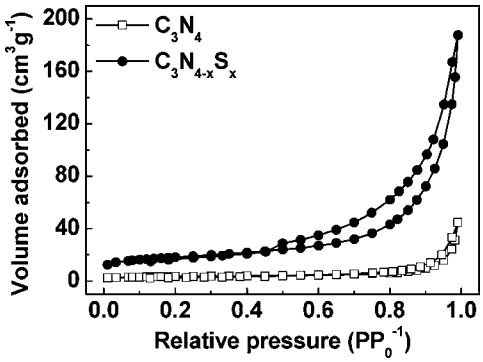

Figure 5. Nitrogen adsorption−desorption isotherms of C_3N_4 and $C_3N_{4-x}S_x$ samples.

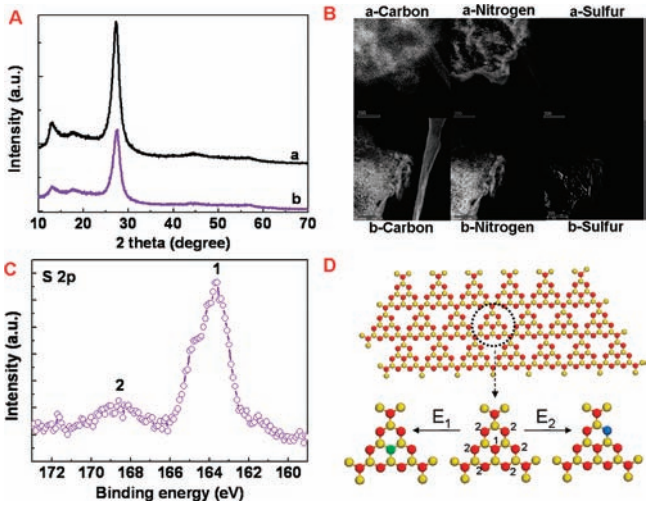

Figure 6. (A) XRD patterns of C_3N_4 (a) and $C_3N_{4-x}S_x$ (b); (B) energy-filtered transmission electron microscopy (TEM) images of carbon, nitrogen, and sulfur in C_3N_4 (a) and $C_3N_{4-x}S_x$ (b); (C) high-resolution XPS spectrum of sulfur recorded from pristine surface of $C_3N_{4-x}S_x$; (D) atomic structure model of a perfect graphitic C_3N_4 sheet consisting of melem units, and two melem units with a substitutional nitrogen atom at different periodic sites by sulfur atom. Carbon, nitrogen, sulfur in site 1 and 2 are indicated by yellow, red, green, and blue spheres.

area from 12 $m^2\ g^{-1}$ for C_3N_4 to 63 $m^2\ g^{-1}$ sulfur-doped C_3N_4 (Figure 5) may be assessed as follows. Although the increased surface area can make an obvious contribution to the absolute hydrogen evolution efficacy of C_3N_4, the normalized efficacy with respect to the specific surface area is usually lowered; for example, according to the data reported by Wang et al.[16f] and Zhang et al.,[16e] the retention percentage of normalized efficacy is less than 100% in mesoporous (8−98%) and proton-activated (53%) C_3N_4 compared to the pristine C_3N_4 under visible light. In our case, the normalized hydrogen evolution rate of $C_3N_{4-x}S_x$ is 152% of C_3N_4 under visible light, though its absorption range is decreased by 0.12 eV to that of C_3N_4. More importantly, the photo-oxidation reaction pathway featuring direct involvement of holes could not be caused simply by increased surface area. The overall enhanced photoreactivity, therefore, can be attributed predominantly to the unique electronic structure acquired with our present doping strategy.

3.3. Origin of Unique Electronic Structure. As described above, the unique electronic structure of the $C_3N_{4-x}S_x$ prepared causes excellent photoreduction and photo-oxidation reactivity. It is therefore important to understand how sulfur doping results in these remarkable properties. XRD patterns of graphitic C_3N_4 (Figure 6A-a), which stacks like graphite with tri-s-triazine-based connection sheet as unit, give two feature diffraction peaks at around 27.3° and 13.1°.[26] After sulfur doping, the unchanged features of the XRD patterns (Figure 6A-b) suggest that the original atomic structure is largely retained. However, the overall diffraction intensity is much weakened, which can be considered to result from a reduced structural correlation length induced by the decreased particle size of $C_3N_{4-x}S_x$.[17] That the particle size is substantially decreased is evidenced both by the apparently much smaller/thinner particles in the TEM image (Figure 7) and the increased specific surface area from 12 to 63 $m^2\ g^{-1}$ (Figure 5). The average particle size measured from Zeta-potential was also decreased from ca. 1 μm to ca. 120 nm. The decrease of the $C_3N_{4-x}S_x$ particle size is one potential factor that may result in the appearance of a larger bandgap, as a consequence of the QCE. Such an effect was invoked previously to explain the observed spectral properties in C_3N_4 nanoparticles by Groenewolt and Antonietti.[27]

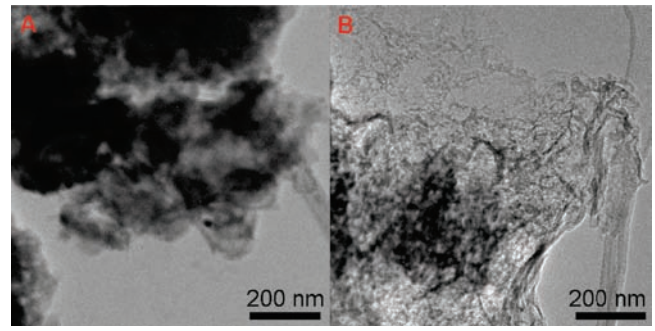

Figure 7. Typical TEM images of C_3N_4 (A) and $C_3N_{4-x}S_x$ (B) particles.

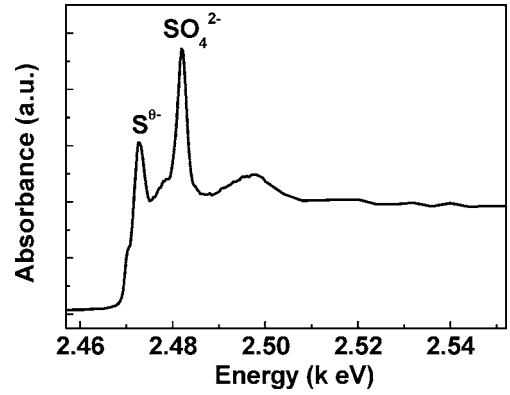

Figure 8. Sulfur K-edge XANES spectrum of $C_3N_{4-x}S_x$ measured in fluorescence mode.

The existence of sulfur within the framework of $C_3N_{4-x}S_x$ is clearly evidenced in the energy-filtered TEM image with strong contrast of S in Figure 6B. The chemical states of sulfur were further revealed by measuring S 2p levels using XPS. Figure 6C shows two S 2p peaks centering at 163.9 and 168.5 eV recorded from the pristine surface of $C_3N_{4-x}S_x$. According to Lindberg et al,[28] the binding energy of S $2p_{3/2}$ in CS_2 was recognized as 163.7 eV. Thus, the peak at 163.9 eV is reasonably considered to be originated from C−S bonds formed in $C_3N_{4-x}S_x$ by substituting sulfur for lattice nitrogen. This conclusion is also supported by XANES spectroscopy. As shown in Figure

(26) Thomas, A.; Fischer, A.; Goettmann, F.; Antonietti, M.; Muller, J. O.; Schlogl, R.; Carlsson, J. M. *J. Mater. Chem.* **2008**, *18*, 4893.
(27) Groenewolt, M.; Antonietti, M. *Adv. Mater.* **2005**, *17*, 1789.
(28) Lindberg, B. J.; Hamrin, K.; Johansson, G.; Gelius, U.; Fahlmann, A.; Nordling, C.; Siegbahn, K. *Phys. Scr.* **1970**, *1*, 286.

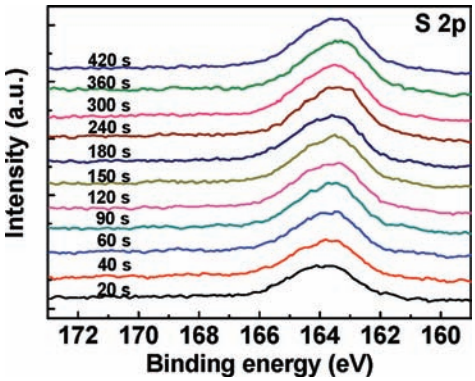

Figure 9. High-resolution XPS spectrum evolution of S 2p in $C_3N_{4-x}S_x$ upon Ar^+ sputtering from 20 to 420 s.

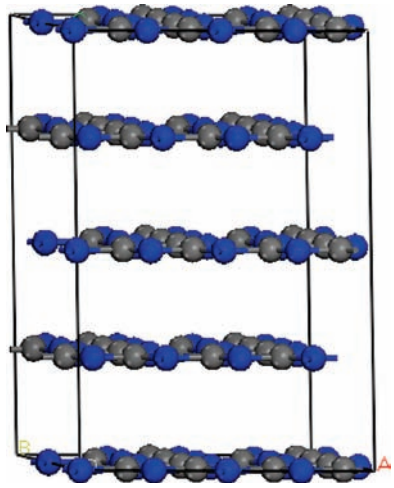

Figure 10. Employed 4 × 4 × 2 supercell (9.48 Å × 9.48 Å × 13.44 Å) with four atomic layers of C_3N_4. C and N are indicated as gray and blue spheres and sulfur dopant is introduced with a two-coordinated nitrogen being replaced by sulfur, resulting in a doping concentration of 1/64.

8, the sulfur K-edge XANES spectrum of $C_3N_{4-x}S_x$ shows two pre-edge features at 2472.6 and 2482.0 eV, which originate from dipole allowed transitions that involve excitation of an 1s electron to antibonding molecular orbitals of sulfur.[29] According to Jalilehvand et al.,[30] these features can be attributed to two different sulfur functional groups, $S^{\theta-}$ ($0 < \theta \leq 2$) and SO_4^{2-}, respectively. The formed $S^{\theta-}$ species exists in $C_3N_{4-x}S_x$ as a result of the replacement of lattice nitrogen atoms with sulfur atoms so that C−S bonds are incorporated into the framework of C−N bonds. Regarding the SO_4^{2-} species detected, it is obvious that surface existing oxygen on C_3N_4 (around 2 at%) can play a key role in capturing sulfur decomposed from H_2S into SO_4^{2-} during doping, which can be indicated by the binding energy shift of O 1s from 530.2 eV in C_3N_4 to 530.0 eV in $C_3N_{4-x}S_x$ (see Figure S3). In addition, it is well-established that the feature intensity of sulfur in different functional groups is very sensitive to the oxidation state of sulfur: the higher the oxidation state, the stronger the feature intensity.[30] This is why the feature intensity of SO_4^{2-} is obviously stronger than that of S^{2-}, though its amount from XPS spectrum is much lower than S^{2-}. However, based on the XPS and XANES spectra, we can only conclude the formation of C−S bonds in the framework of C−N bonds by replacement of lattice N with S, but still can not recognize the exact position of substitutional sulfur for nitrogen.

The atomic structure model of a perfect graphitic C_3N_4 consisting of melem units is given in Figure 6D. Two groups of periodic nitrogen atoms exist in the melem unit, as numbered with 1 and 2. A question then arises: are both groups of periodic nitrogen atoms favorable for substituting? The formation energy (E) of substitutional sulfur for nitrogen was first calculated by replacing one nitrogen atom in site 1 or 2 with sulfur. E_1 and E_2 for site 1 and 2 are 7.26 and 3.41 eV, respectively, suggesting that site 2 is energetically favorable for substitutional doping. In combination with the advantages of high percentage (6:1) and weak steric effect of site 2, the substitutional sulfur for nitrogen in site 2 should be overwhelming with respect to site 1.

The ratio of substitutional sulfur to nitrogen was around 1.1 at%. At this doping level, the binding energy of C 1s and N 1s is exposed to a slight shift by ca. 0.1 eV toward low energy (Figure S4 in Supporting Information). The weak peak 2 at higher energy exists only on the surface of $C_3N_{4-x}S_x$ and totally disappears after 20 s Ar^+ sputtering, again suggesting that it comes from surface adsorbed sulfur species SO_4^{2-}. The nearly unchanged peak position and area of S 2p upon long time

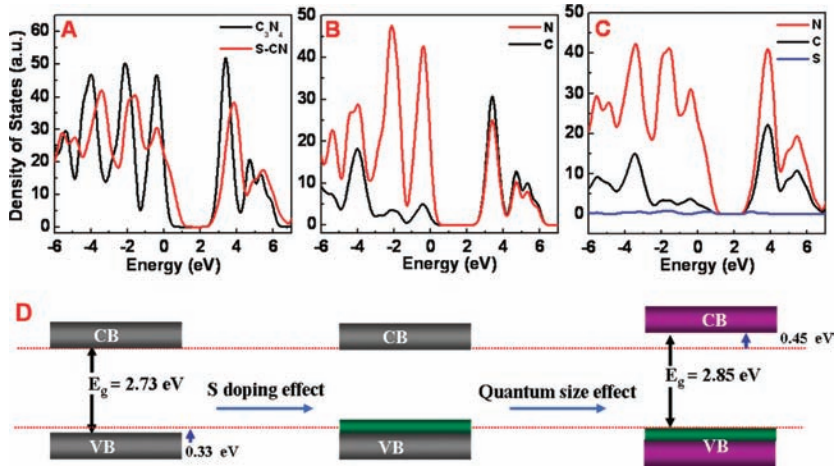

Figure 11. (A) Total DOSs of C_3N_4 (black line) and $C_3N_{4-x}S_x$ (red line); (B) the projected DOSs of nitrogen (red line) and carbon (black line) of C_3N_4; (C) the projected DOSs of nitrogen (red line), carbon (black line), and sulfur (blue line) of $C_3N_{4-x}S_x$. The dopant sulfur is located at a substitutional site for 64 nitrogen atoms in the employed 4 × 4 × 2 periodic model. (D) Schematic of band structure evolution of C_3N_4 by sulfur doping effect and subsequent quantum confinement effect.

sputtering (Figure 9) indicate the homogeneous distribution of sulfur within the whole particles.

The effect of sulfur doping alone in site 2 on the electronic structure of $C_3N_{4-x}S_x$ was theoretically investigated. In our calculation, C_3N_4 is modeled by a $4 \times 4 \times 2$ supercell (9.48 Å $\times$ 9.48 Å $\times$ 13.44 Å) with four atomic layers of C_3N_4, as shown in Figure 10 (C and N indicated as gray and blue spheres). Sulfur dopants were introduced with a two-coordinated nitrogen being replaced by sulfur, resulting in a doping concentration of 1/64. During the geometric optimization, no atom was fixed, except that lattice parameters were fixed to experimental values. The key insight derived from the calculation results (Figures 11A−C) is that the substitutional doping of S is effective in both narrowing the bandgap and increasing VB width of C_3N_4 by the interaction of S 3p states with N 2p states. The trend of increasing VB width here well matches with the experimental result. However, the experimentally measured bandgap of $C_3N_{4-x}S_x$ actually increases by 0.12 eV with respect to C_3N_4. This contradiction can apparently be rationalized by considering the role of QCE, induced by the decreased particle size, in widening bandgap through oppositely shifting VB and CB edges. This is indicated schematically in Figure 11D.

4. Conclusions

Homogeneously sulfur-doped graphitic C_3N_4 was prepared, and it shows a photoreactivity of H_2 evolution 7.2 and 8.0 times higher than C_3N_4 under $\lambda > 300$ and 420 nm, respectively. More strikingly, the complete oxidation process of phenol under $\lambda >$ 400 nm can occur for the sulfur-doped C_3N_4, which is impossible for C_3N_4 even under $\lambda > 300$ nm. The remarkable photocatalytic performance of the sulfur-doped graphitic C_3N_4 is considered to be a synergistic consequence of a widening and upshifting of the VB, achieved through homogeneous distribution of the dopant sulfur, and an upshifting of the CB minimum caused by the QCE relating to the markedly reduced particle size after doping. As supported by both experimental and theoretical characterizations, these features result collectively in a unique electronic structure which is highly efficient in promoting visible light responsive photo-oxidation and photoreduction processes.

Acknowledgment. We thank Prof. Erdong Wu for the valuable discussion on XANES. The financial support from Major Basic Research Program, Ministry of Science and Technology of China (No. 2009CB220001), NSFC (No. 50921004), Solar Energy Initiative of the Chinese Academy of Sciences (CAS), CAS funding (No. KJCX2-YW-H21-01), China Postdoctoral Science Foundation funded project (No. 20100471486) and the IMR SYNL-T.S. Kê Research Fellowship is gratefully acknowledged.

Supporting Information Available: The emission spectrum of the Xe lamp employed, XPS spectra of N 1s, C 1s and S 2p in $C_3N_{4-x}S_x$ before and after reaction, XPS spectra of O 1s, C 1s and N 1s in C_3N_4 and $C_3N_{4-x}S_x$. This material is available free of charge via the Internet at http://pubs.acs.org.

JA103798K

(29) George, G. N.; Gorbaty, M. L. *J. Am. Chem. Soc.* **1989**, *111*, 3182.
(30) Jalilehvand, F. *Chem. Soc. Rev.* **2006**, *35*, 1256.